

# Stability studies on subtractively-fabricated CMOS-compatible superconducting transmon qubits

Chawki Dhib, <sup>1,\*</sup> Johannes Weber, <sup>1</sup> Samuel Taubenberger, <sup>1</sup> Carla Morán Guizán, <sup>1</sup> Simon J. K. Lang, <sup>1</sup> Zhen Luo, <sup>2</sup> Emir Music, <sup>1</sup> Alwin Maiwald, <sup>1</sup> Wilfried Lerch, <sup>1</sup> Lars Nebrich, <sup>1</sup> Marc Tornow, <sup>1,2</sup> Thomas Mayer, <sup>1</sup> Daniela Zahn, <sup>1</sup> Rui N. Pereira, <sup>1</sup> and Christoph Kutter<sup>1,3</sup>

<sup>1</sup>*Fraunhofer Institut für Elektronische Mikrosysteme und Festkörpertechnologien EMFT, Munich, Germany*

<sup>2</sup>*School of Computation, Information and Technology, Technical University of Munich, Munich, Germany*

<sup>3</sup>*Center Integrated Sensor Systems (SENS), Universität der Bundeswehr München, Munich, Germany*

(Dated: December 23, 2025)

Developing fault-tolerant quantum processors with error correction demands large arrays of physical qubits whose key performance metrics (coherence times, control fidelities) must remain within specifications over both short and long timescales. Here we investigated the temporal stability of subtractively fabricated CMOS-compatible superconducting transmon qubits. During a single cooldown and over a period of 95 hours, we monitored several parameters for 8 qubits, including coherence times  $T_1$  and  $T_2^*$ , which exhibit fluctuations originating primarily from the interaction between two-level system (TLS) defects and the host qubit. We also demonstrate that subtractively-fabricated superconducting quantum devices align with the theoretical predictions that higher mean lifetimes  $T_1$  correspond to larger fluctuations. To assess long-term stability, we tracked two representative qubits over 10 cooldown cycles spanning more than one year. We observed an average total downward shift in both qubit transition frequencies of approximately 61 MHz within the thermal cycles considered. In contrast, readout resonator frequencies decreased only marginally. Meanwhile,  $T_1$  exhibits fluctuations from cycle to cycle, but maintains a stable baseline value.

## I. INTRODUCTION

Developing a fault-tolerant quantum computer implementing quantum error correction (QEC) requires a large number of physical qubits with consistently high-quality metrics [1, 2]. To scale to such large QPUs, it is advantageous to move away from lift-off techniques to facilitate processing of larger wafers, e.g., with diameters up to 8 or 12 inch. Industrial-grade, CMOS-compatible qubit fabrication processes are suitable for large wafers and promise high precision and reproducibility. Previous works have demonstrated the feasibility of producing superconducting qubit wafers with high yield using only CMOS-techniques [3–6]. For QEC, the qubit parameters must also satisfy several requirements: high coherence times to provide enough headroom for QEC-cycles, and high readout and gate fidelities allowing precise control [1, 7, 8]. An equally critical performance metric that must be considered is the temporal stability of these parameters. If any of the parameters of a qubit or several qubits fall below the required thresholds during operation or between cooldown cycles, the QPU’s performance can be compromised [9, 10]. Qubits made with lift-off-techniques have been shown to exhibit fluctuations in key parameters, namely  $T_1$  and  $T_2$  [11–15].

In this work, we systematically study the temporal stability of our subtractively fabricated

qubits, using a design with minimal noise sources over a period of approximately 95 hours during a single cooldown, and we investigate instabilities driven primarily by two-level system (TLS) defects. We demonstrate that these subtractively fabricated qubits exhibit the same degree of  $T_1$  stability as qubits made with lift-off methods. We also report on the variation of several qubit parameters ( $T_1$ , qubit and readout frequencies) between multiple cooldown cycles, spanning more than a year in total.

## II. EXPERIMENT

The devices studied here are test transmon qubits that stem from two chips (A and B) from the same wafer, which was fabricated using the method described in [5]. For our test chip layout, we omit dedicated drive lines and rely solely on readout resonators to both drive and read out the qubits. As conceptually depicted in Fig. 1, each chip contains 4 qubits plus one reference resonator. Tab. I summarizes the design parameters of these qubits: readout resonator frequency  $f_r$ , qubit frequency  $f_q$ , and anharmonicity. The cryogenic setup is described in detail in Fig. 2.

We investigate parameter stability of the 8 qubits listed in Tab. I over 95 hours during a single cooldown, where we perform for each qubit a lifetime measurement, a Ramsey experiment, and a single-shot readout experiment. Tab. II lists the measured parameters, their definitions and the experiments from which they were extracted. A

\* [chawki.dhib@emft.fraunhofer.de](mailto:chawki.dhib@emft.fraunhofer.de)

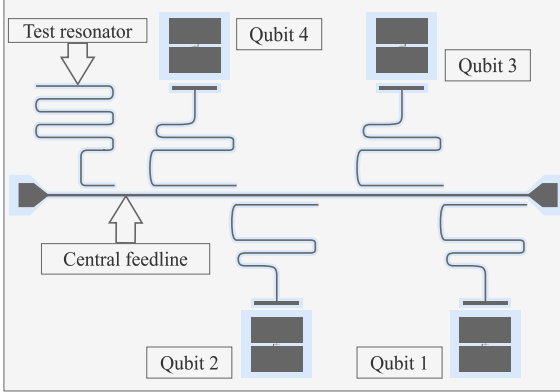


Fig. 1. Sketch of a single-qubits chip layout with 4 qubits structures and a test resonator coupled to a central feedline.

Tab. I. Frequency parameters of measured qubits

Chip	Qubit	$f_r$ (GHz)	$f_q$ (GHz)	Anharmonicity (MHz)
A	1	6.5829	4.332736	225.075
A	2	6.7383	4.320850	219.487
A	3	6.9860	4.563595	228.126
A	4	7.1407	4.671054	220.046
B	1	6.5849	4.441636	224.806
B	2	6.7367	4.541780	223.012
B	3	6.9749	4.164750	228.386
B	4	7.1428	4.621970	228.406

more detailed description of the pulse sequences and parameters extraction can be found in the supplementary information (S.I. I.). For a single qubit, each measurement cycle (lifetime measurement + Ramsey experiment + single-shot readout experiment) takes between 64 s and 130 s, depending on  $T_1$ . Qubits on the same chip are probed sequentially. Both chips are characterized in parallel using two separate sets of measurement instruments which are placed outside the dilution refrigerator (DR) in a non-temperature-stabilized environment. Additionally, we monitor the temperature of the mixing chamber (MXC) of the DR using a RuO<sub>2</sub>-temperature sensor (see Fig. 2). The Ramsey experiment was carried out with a fixed detuning  $\Delta_f$ , introduced by adding a phase to the second pulse, and without modifying the calibrated drive frequency (see S.I. I.B.2 for further details). The results of this 95-hour single-cooldown stability analysis are presented in section III A.

Beyond evaluating stability over several days and during a single cooldown, we also examine qubit stability over extended timescales spanning multiple cooldowns. We track both resonator and qubit frequencies for two representative qubits, A.1 and B.1, along with their lifetimes  $T_1$ , across 10 cooldown cycles over more than a year (other

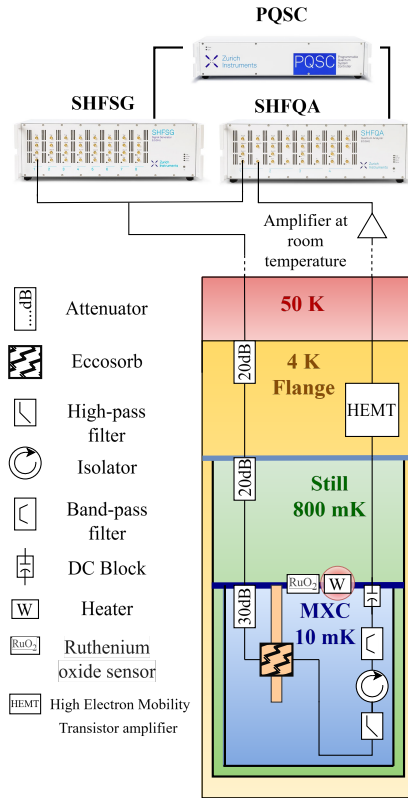


Fig. 2. Illustration of the cryogenic measurement setup. The qubit chips are mounted in the mixing chamber (MXC) of a Bluefors LD dilution refrigerator (DR), enclosed in a copper package and covered with Eccosorb. The MXC temperature is monitored with a RuO<sub>2</sub>-temperature sensor. Drive and input readout signals are generated respectively by a signal generator (SHFSG) and a quantum analyzer (SHFQA), synchronized by a PQSC (all from Zurich Instruments). Both signals go through a combiner at room temperature and then are attenuated at each stage of the DR to suppress thermal noise. The output readout signal passes through filters and isolators before being amplified at the 4K stage and at room temperature.

qubits were monitored but over fewer cooldowns). Each cooldown lasts between 7 and 30 days and is followed by a warm-up and a vacuum break of the dilution refrigerator, during which the qubit chips remain inside their cryo-packages in ambient air. The 95-hour measurement corresponds to the fifth cooldown in this series. The results of this long-term stability study are presented in section III B.

### III. RESULTS

#### A. Single-cooldown stability over ca. 95 h

As described in the previous section, the stability over 95 hours was analyzed for 8 qubits in

Tab. II. Description of performed experiments and extracted parameters

Experiment	Description	Parameter	Definition
Lifetime measurement	X <sub>180</sub> -delay-readout sequence	$T_1$	Longitudinal relaxation time, time constant of the exponential decay fit.
Ramsey	X <sub>90</sub> -delay-X <sub>90</sub> -readout sequence	$T_2^*$	Effective transverse relaxation time, time constant of the oscillatory decay fit.
		$ f_{\text{Ramsey}} $	Absolute value of the frequency of Ramsey oscillations.
Single-shot readout	$N$ times readout of the qubit at ground state, $N$ times readout of the qubit at excited state. When the readout results are plotted in the IQ plane, two blobs are observed (ideally). In our case, $N = 2^{12}$ .	$\Delta_m$	The distance between the means of the IQ blobs.
		$\mathcal{F}$	Readout fidelity, calculated after state discrimination.
		$T_{\text{eff}}$	Effective temperature of the qubit, calculated based on the results of state discrimination.

total. As an example, [Fig. 3](#) shows the results for qubit A.2. The left panels show the time evolution of the measured parameters, and the right panels display their corresponding distribution histograms. The bottom panel ([Fig. 3.g](#)) shows the time evolution of the MXC temperature,  $T_{\text{MXC}}$ .

The histograms of  $T_1$  and  $T_2^*$  ([Fig. 3.a,b](#)) exhibit a negative skewness. This skewness originates from abrupt and aperiodic drops in the time evolution of  $T_1$  and  $T_2^*$ . These drops vary in duration and magnitude and are primarily attributed to spectral diffusion caused by crossings of two-level system (TLS) defects over the qubit frequency [[12, 16–18](#)]. The  $T_1$  drops coincide with those of  $T_2^*$ , as shown by the red intervals in [Fig. 3.a,b](#), and as expected from  $1/T_2 = 1/(2T_1) + 1/T_\varphi$  and  $T_2^* \leq T_2$  [[19, 20](#)]. To properly describe the skewness observed in the histograms of  $T_1$  and  $T_2^*$ , we use a Rician fit with an offset (see S.I. II.B).

Through  $|f_{\text{Ramsey}}| - \Delta_f$  ([Fig. 3.c](#)), we can track the time evolution of the qubit frequency. The qubit frequency exhibits both abrupt jumps as well as drifts. It has been observed in [[16](#)] that TLS defects can also undergo either sudden frequency changes (telegraphic) or frequency drifts (diffusive). Since TLS can interact with the qubit and shift its frequency via hybridization [[21–24](#)], the observed qubit frequency changes could be caused by energy changes of nearby TLS [[13](#)]. In total, the observed frequency shift was small (below 15 kHz).

Next, we analyze the single-shot readout results. [Fig. 3.d](#) shows that  $\Delta_m$  undergoes noticeable but small variations throughout the experiment, which are discussed in the next section. The readout fidelity  $\mathcal{F}$  ([Fig. 3.e](#)) was relatively stable for A.2 during the measurement period.

The effective qubit temperature  $T_{\text{eff}}$  ([Fig. 3.f](#)) behaves similarly as the readout fidelity, which is expected because they are related (see S.I. I.B.3).  $T_{\text{eff}}$  shows no correlation with the steadily decreasing  $T_{\text{MXC}}$  ([Fig. 3.g](#)). This is in agreement with previous findings [[25–27](#)] that at low mixing-chamber temperatures, the qubit's effective temperature remains independent of  $T_{\text{MXC}}$ .

#### Comparison between qubits

Next, we investigate how the different parameters compare between different qubits. [Fig. 4](#) displays the parameter changes for all measured qubits. From  $T_2^*$  results, we exclude qubit A.1, due to inadequate detuning during a  $T_2^*$  decrease and a too small measurement window after an increase in  $T_2^*$  later on. We also omit the  $\Delta_m$  results for B.3, due to strong fluctuations (see S.I. II.C.1).

In [Fig. 4.a](#), the  $T_1$  time traces show that  $T_1$  drops can vary significantly in magnitude across qubits. Some qubits exhibit significant decreases of  $T_1$  below 50%, or in the worst case scenario below 10%, of its original value while others remain stable. As expected, these pronounced  $T_1$  drops are mirrored in the  $T_2^*$  traces ([Fig. 4.b](#)).

The most significant decrease affected B.1 (green dotted lines in [Fig. 4.a-e](#)). Within this time interval, in addition to  $T_2^*$  and  $T_1$ ,  $\Delta_m$  and  $\mathcal{F}$  also decreased due to decay during readout. Such drastic qubit performance decreases (dropouts) have been previously observed [[11, 13, 28](#)]. They are generally attributed to interactions with strongly coupled TLS and can in principle affect any qubit, occurring stochastically such that extended measurement time spans are more likely to capture these events. Such events can significantly affect QPU operation. Mitigation strategies include decreasing the size of

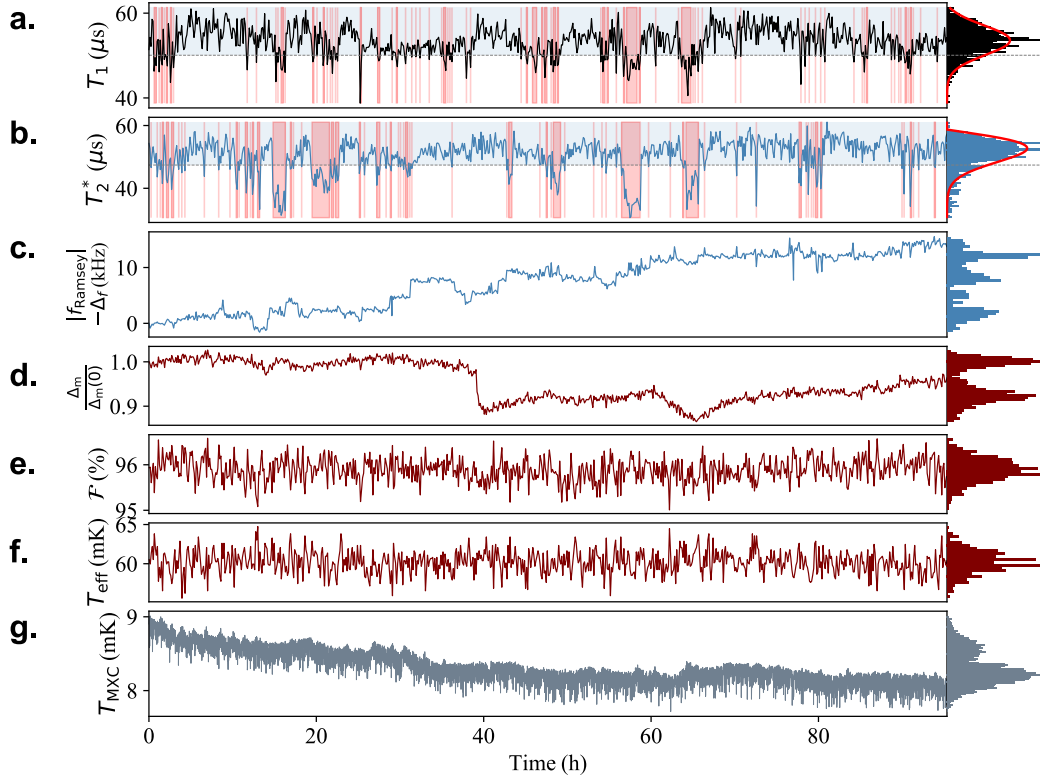


Fig. 3. Results of 95-hour single-cooldown measurements for qubit A.2, with time traces on the left and corresponding histograms on the right in each panel: a)  $T_1$ , b)  $T_2^*$ , c)  $|f_{\text{Ramsey}}| - \Delta_f$ , where  $\Delta_f$  is the set detuning, d)  $\Delta_m$ , e) readout fidelity  $\mathcal{F}$ , f)  $T_{\text{eff}}$ , and g)  $T_{\text{MXC}}$ . The red curves in histograms (a) and (b) represent fits using a Rician distribution with an offset. This choice of fit function allows to describe the observed skewness. Note that this choice is purely empirical and is not derived from an underlying physical model. The fits are used to determine the mean and standard deviation via integration. The red-shaded regions in (a) and (b) indicate where  $T_1$  or  $T_2^*$  fall more than one standard deviation below the mean (threshold marked by the dotted horizontal gray lines). These red-shaded regions highlight the simultaneous drops of  $T_1$  and  $T_2^*$ .

the Josephson junction [29], using flux-tunable qubits, or TLS control strategies [24, 30–32].

We notice that qubit A.1 experienced similar decreases (blue dashed lines in Fig. 4.c-e). However, during the corresponding time interval, no decrease in its  $T_1$  was observed. Further investigation is required to explain this behavior.

Regarding the qubit frequency (see Fig. 4.c) no correlation with other parameters was observed, except for B.1 and A.1 during specific intervals and B.4, where the main frequency jumps coincide with jumps in  $T_2^*$ . During the times where we could determine the frequency reliably,  $|f_{\text{Ramsey}}| - \Delta_f$  remains below 100 kHz, indicating minimal variations of the qubit frequencies and reliable stability.

Furthermore, Fig. 4.e demonstrates that the readout fidelity  $\mathcal{F}$  remains consistently high for all qubits, apart from A.1 and B.1 during specific intervals, during which also  $\Delta_m$  dropped. Otherwise, changes of  $\Delta_m$  remain small (see Fig. 4.d), reaching a maximum of approximately -13.7%. Fig. 4.d also reveals that the traces of

$(\Delta_m(t) - \Delta_m(0))/\Delta_m(0)$  follow similar temporal profiles across qubits with some offsets. This finding implies that although the baseline values of  $\Delta_m$  differ among qubits, its temporal variations arise from common factors shared between the chips. Since the correlation between the  $T_{\text{MXC}}$  and  $\Delta_m$  is weak and the chips have separate measurement paths, we attribute the  $\Delta_m$  changes to influence(s) of the environment(s) in which components of the measurement setup (wiring, amplifiers, measurement instruments) are placed.

#### **$T_1$ stability**

To benchmark our qubits in terms of  $T_1$ -stability, we systematically compare results of measurements performed on devices fabricated using similar or different methods. The following section provides, to the best of our knowledge, for the first time a systematic benchmarking of the long-term  $T_1$  stability of CMOS-compatible subtractively fabricated qubits compared to lift-off fabricated qubits.

For this study, we include only datasets where

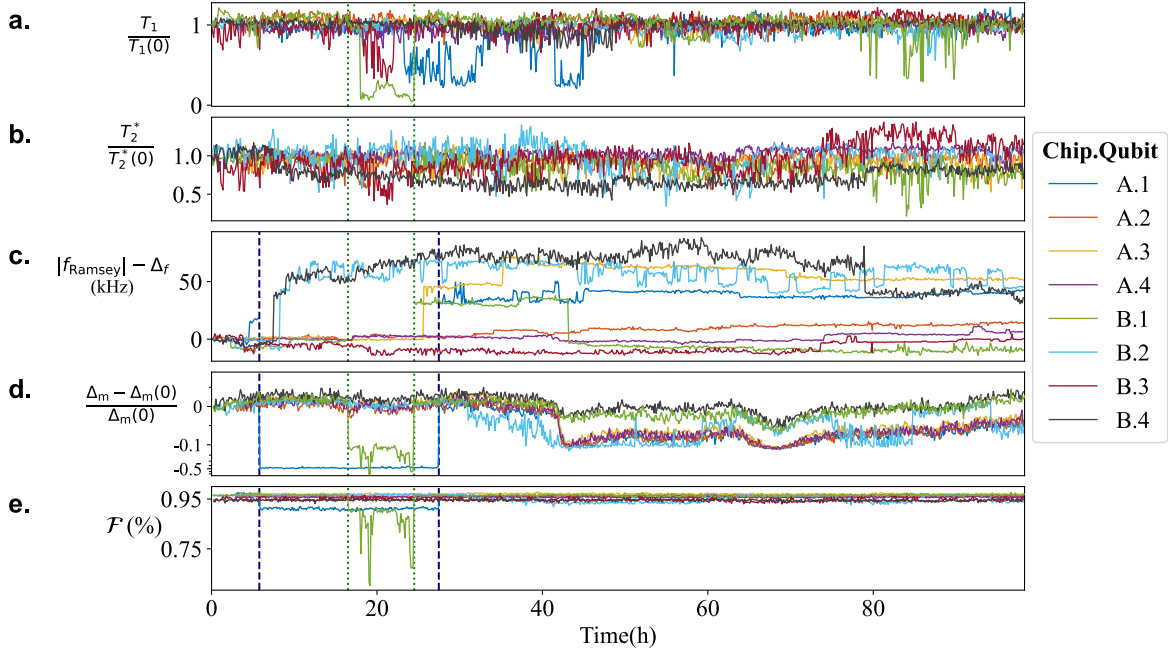


Fig. 4. Temporal evolution of a)  $T_1(t)/T_1(0)$ , b)  $T_2^*(t)/T_2^*(0)$ , c)  $|f_{\text{Ramsey}}| - \Delta_f$ , d)  $\frac{\Delta_m(t) - \Delta_m(0)}{\Delta_m(0)}$ , and e) readout fidelity  $\mathcal{F}$  for all qubits (except Ramsey results of A.1 and  $\Delta_m$  results for B.3). Panel (d) uses a logarithmic scale on the y-axis with a linear interval  $\pm 0.1$  around 0. The green dotted lines indicate the time limits of the largest  $T_1$  drop observed in qubit B.1, and highlight its impact on the other parameters. Due to  $T_2^*$  decrease, the Ramsey results were unreliable during this time interval and therefore omitted. The blue dashed lines delimit the time interval where the readout fidelity and  $\Delta_m$  decreased for A.1 and the Ramsey frequency could not be determined due to  $T_2^*$  decrease.

the original authors provided raw data or distributions of  $T_1$ . We also require that the datasets contain more than 500 points collected over at least 10 hours and during a single cooldown. These requirements are put to ensure statistical reliability and properly reflect the dynamics of  $T_1$ . For each qubit, we determine the mean and standard deviation of the corresponding  $T_1$  distribution by fitting the histograms (Rician distribution fit) and computing the integrals. We use integration for mean and variance calculations to avoid the influence of extreme and prolonged outliers (dropouts), which, as mentioned, do not necessarily affect every qubit during a given time interval. Here, we focus on the general  $T_1$  stability (excluding dropout events).

The considered datasets for the benchmarking use three different fabrication approaches: (i) a CMOS-compatible subtractive process (EMFT, IMEC [6]), (ii) the Dolan bridge method (Chalmers [12], WMI [11], Müller et al./IBM [14]), and (iii) the Manhattan method (VTT [15], EPFL [13]). Both Dolan and Manhattan are lift-off methods. Our own dataset (EMFT) comprises three subsets: EMFT\_0, consisting of the 8 qubits analyzed in this work; EMFT\_1, with additional chips from the same process run as EMFT\_0 [5]; and EMFT\_2, with chips from a subsequent

run [4]. All the mentioned works employ Al/Al-Ox/Al Josephson junctions. All structures other than the Josephson junction are made from aluminum, except for WMI, EPFL, and VTT where, e.g., resonators or shunted capacitors are made of Nb.

In Fig. 5, we plot the standard deviations  $\sigma_{T_1}$  with respect to the corresponding average lifetimes  $\langle T_1 \rangle$ . Fig. 5 shows that all qubits considered follow a common trend where higher average lifetimes  $\langle T_1 \rangle$  correspond to higher standard deviations  $\sigma_{T_1}$ . This finding is in agreement with previous results [12, 33, 34] and the theoretical model derived from [30] where:

$$\sigma_{T_1} = a \cdot \langle T_1 \rangle^{\frac{3}{2}} \quad (1)$$

with  $a$  being a proportionality factor related to fluctuations of the decay caused by a single TLS (see S.I. II.C.2) This model assumes that TLS defects are the dominant source of energy relaxation [30]. We find that all qubits, regardless of the fabrication method, can be described with the same proportionality factor  $a$ .

The observed relation between  $\langle T_1 \rangle$  and  $\sigma_{T_1}$ , suggests that as the qubit lifetimes increase, the stability decreases, which needs to be taken into account when using the QPU. In addition, the

experimental results show that qubits fabricated with our subtractive CMOS-compatible approach are as stable as superconducting qubits fabricated with the traditional lift-off methods.

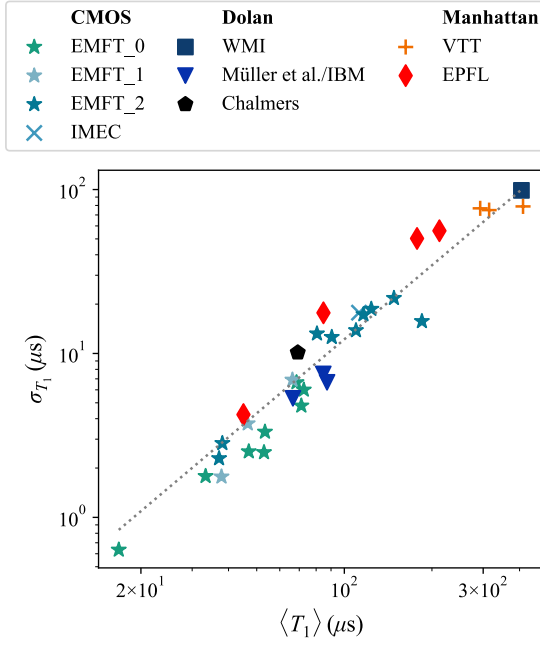


Fig. 5. Standard deviation of  $T_1$  with respect to its mean value, logarithmically scaled. The dotted line represents the fit following Eq. 1 which gives for  $a = (1.220 \pm 0.052) \times 10^{-2} \text{ s}^{\frac{2}{3}}$ .

### B. Long-term stability (over several cooldowns)

Two qubits from chips A and B were measured across 10 cooldowns over the course of one year. Fig. 6 summarizes the results, with each data point corresponding to one cooldown.

Each point in Fig. 6.a corresponds to the average  $T_1$  for a given cooldown.  $T_1$  fluctuates between cooldowns, but remains within bounds around a stable value. This behavior of  $T_1$  can be attributed to a reconfiguration of the spectrum of TLS defects due to thermal cycling [29, 35, 36].

Fig. 6.b shows the qubit frequency shifts  $\Delta f_q$  relative to the first cooldown. There is a gradual decrease which appears to saturate toward the end of the measurement series and amounts to around 50-70 MHz in total.

The observed decrease in  $f_q$  can be explained by an increase in the room temperature resistance of the junction  $R_N$ , as shown by previous aging studies [37–40]. A higher  $R_N$  reduces the Josephson energy  $E_J \propto 1/R_N$ . Consequently, the transi-

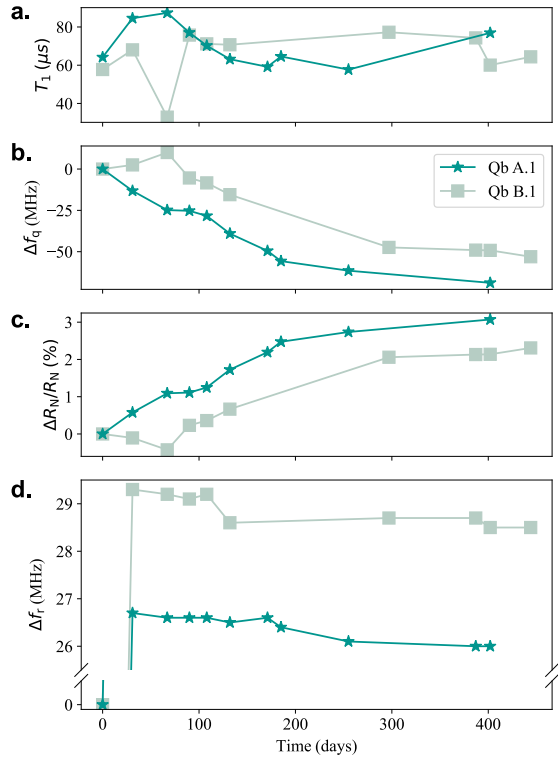


Fig. 6. Evolution over multiple cooldown cycles of a)  $T_1$  and of b) qubit and d) readout frequencies compared to their initial values ( $\Delta f_q$  and  $\Delta f_r$ ). c) Evolution of estimated  $\Delta R_N/R_N$ .

sition frequency decreases as follows [41]:

$$f_q \approx \frac{1}{h} \left( \sqrt{8E_J E_C} - E_C \right) \quad \text{for} \quad \frac{E_J}{E_C} \gg 1 \quad (2)$$

where  $E_C$  is the charging energy of the Josephson junction and  $h$  is the Planck constant. The increase in  $R_N$  has been attributed to a gradual, slow, and correlated rearrangement of the crystal structure of the aluminum oxide barrier at room temperature. Over time, traps states at the metal-oxide interface relax and reconfigure towards deeper potential minima, thereby increasing the barrier thickness [37]. If the barrier is contaminated with resist residues or hydrates, and not cleaned properly, the aging and variation of the resistance and qubit frequency are more pronounced [38–40].

To quantify the variation that could have occurred to  $R_N$ , we calculate it based on our values of  $f_q$  and the following expression derived from Eq. 2, and  $E_J = h\Delta/(8e^2 R_N)$  [41, 42]:

$$R_N = \frac{h\Delta E_C}{e^2(f_q \cdot h + E_C)^2}. \quad (3)$$

$\Delta$  is the superconducting gap and  $e$  is the elementary charge. Using our previously determined

critical temperature  $T_c$  [5] to calculate  $\Delta$ , and the values of anharmonicities in [Tab. I](#), we obtain the results shown in [Fig. 6.c](#).

On average, the measured qubits maintained  $\Delta R_N/R_N$  below 3.4% over 400 days, which is lower than the aging observed for junctions fabricated with lift-off methods [6, 36–38]. We acknowledge that direct comparison between different technologies and setups is challenging due to variations in the time elapsed between fabrication completion and initial characterization (approximately 27 days in our case), as well as the slowing-down of aging during cooldown [37]. We hypothesize that the low aging we observe from our qubits is due to the resist removal step using  $O_2$ -plasma at 250 °C [5, 38].

Similarly to  $\Delta f_q$ , [Fig. 6.d](#) shows the resonator frequency shift  $\Delta f_r$  with respect to the first cooldown. There is a pronounced jump between the first and second cooldowns for both qubits. All qubits on chips A and B experience this jump in their readout frequencies (see [S.I. III](#)). We also confirm that this change affected the test resonators (see [Fig. 1](#)) and the bare readout resonance frequencies. Interestingly, this jump was limited to chips A and B; other chips from the same wafer show only slight frequency decreases. The origin of this initial shift remains unclear. Subsequent decreases of  $f_r$  in later cooldowns can be caused by changes of the bare resonator frequency  $f_{r,\text{bare}}$  as well as changes of  $f_q$  and the qubit-resonator coupling  $g$  [43–46]:

$$f_r \approx f_{r,\text{bare}} + \frac{g^2}{f_{r,\text{bare}} - f_q}. \quad (4)$$

As  $g \propto (1/R_N)^{1/4}$  and  $f_q \propto (1/R_N)^{1/2}$ , an increase of  $R_N$  leads to a decrease of  $f_r$ . We estimate that this effect accounts for roughly 25 % of the observed changes, and 75 % from decreases of  $f_{r,\text{bare}}$ . The latter might stem from an increase of the effective dielectric permittivity  $\epsilon_{\text{eff}}$  possibly due to material changes, or an increase in  $l_{\text{tot}}$  due to cracks formation and/or growth in the aluminum resonator induced by thermal cycling [47]. These changes affect  $f_{r,\text{bare}}$  following the equation [48, 49]:

$$f_{r,\text{bare}} \approx \frac{c_0}{4l_{\text{tot}} \cdot \sqrt{\epsilon_{\text{eff}}}} \quad (5)$$

$c_0$  denotes the vacuum light speed.

#### IV. SUMMARY AND DISCUSSION

Our results from measurements over a 95-hour period and during a single cooldown demonstrate that subtractively fabricated CMOS compatible superconducting qubits can achieve parameter

stability on par with lift-off devices, while offering high yield, long lifetimes, and the scalability advantages of industry-grade CMOS processes [4, 5]. The observed superlinear scaling  $\sigma_{T_1} \propto \langle T_1 \rangle^{3/2}$  combined with our observations on  $T_1$  temporal evolution confirm that the TLS-qubit interactions remain the limiting factor for  $T_1$  stability even at higher lifetimes. TLS defects might also influence the qubit frequency or indirectly other performance metrics (e.g. increased decay during readout, which reduces readout fidelity). We also acknowledge the possibility of  $T_1$ -dropouts in superconducting qubits, which can heighten the error probability in a QPU. These findings underscore the need for improved materials and surface treatments that mitigate the TLS effects, or for stabilizing strategies that circumvent existing TLS [24, 30–32]. Additional mechanisms may also contribute to instabilities of some qubit parameters.

Our measurements over 10 cooldowns spanning more than a year show that  $T_1$  (in mean value) is subject to fluctuations due to thermal cycling but retains a stable baseline. Qubit frequencies  $f_q$  experience a gradual decrease, driven by an increase in the room temperature resistance  $R_N$  of the Josephson junction. However, this aging effect is moderate: the computed  $R_N$  values show  $\Delta R_N/R_N$  of only 3.4% on average over 400 days. Nevertheless, such variations should ideally be minimized or accounted for in future QPUs undergoing multiple thermal cycles.

In summary, our benchmarking and long-term stability studies validate the viability of subtractively fabricated CMOS-compatible superconducting qubits for scalable quantum processors, while pinpointing the key challenges that must be addressed to achieve large-scale fault-tolerant devices.

#### ACKNOWLEDGMENTS

The authors would like to thank Tianmu Zhang and Lukas Sigl from Zurich Instruments for their helpful support in setting up the qubit measurement system. We acknowledge helpful discussions and assistance with test chip design and setting up of cryogenic measurements from G. Huber, I. Tsitsilin, F. Haslbeck and C. Schneider from the Quantum Computing group at the Walther Meissner Institute. We also appreciate the whole Fraunhofer EMFT clean room staff for the professional fabrication.

This work was funded by the Munich Quantum Valley (MQV) – Consortium Scalable Hardware and Systems Engineering (SHARE), funded by the Bavarian State Government with funds from the Hightech Agenda Bavaria, the Munich

Quantum Valley Quantum Computer Demonstrator - Superconducting Qubits (MUNIQC-SC) 13N16188, funded by the Federal Ministry of Education and Research, Germany, and the Open

Superconducting Quantum Computers (OpenSuperQPlus) Project - European Quantum Technology Flagship.

---

[1] R. Acharya, D. A. Abanin, L. Aghababaie-Beni, I. Aleiner, T. I. Andersen, M. Ansmann, F. Arute, K. Arya, A. Asfaw, N. Astrakhantsev, *et al.*, *Nature* (2024).

[2] J. M. Gambetta, J. M. Chow, and M. Steffen, *npj quantum information* **3**, 2 (2017).

[3] T. Mayer, H. Bender, S. Lang, Z. Luo, J. Weber, C. M. Guizan, C. Dhib, D. Zahn, L. Schwarzenbach, W. Hell, *et al.*, arXiv preprint arXiv:2505.04337 (2025).

[4] T. Mayer, J. Weber, E. Music, C. M. Guizan, S. Lang, L. Schwarzenbach, C. Dhib, B. Kiliar, A. Maiwald, Z. Luo, *et al.*, arXiv preprint arXiv:2505.08424 (2025).

[5] S. Lang, T. Mayer, J. Weber, C. Dhib, I. Eisele, W. Lerch, Z. Luo, C. M. Guizán, E. Music, L. Sturm-Rogon, *et al.*, *Physical Review Applied* **24**, 054052 (2025).

[6] J. Van Damme, S. Massar, R. Acharya, T. Ivanov, D. Perez Lozano, Y. Canvel, M. Demarets, D. Vangoidsenhoven, Y. Hermans, J. Lai, *et al.*, *Nature* **634**, 74 (2024).

[7] H. Puttermann, K. Noh, C. T. Hann, G. S. McCabe, S. Aghaeimeibodi, R. N. Patel, M. Lee, W. M. Jones, H. Moradinejad, R. Rodriguez, *et al.*, *Nature* **638**, 927 (2025).

[8] A. G. Fowler, M. Mariantoni, J. M. Martinis, and A. N. Cleland, *Physical Review A—Atomic, Molecular, and Optical Physics* **86**, 032324 (2012).

[9] S. Sheldon, L. S. Bishop, E. Magesan, S. Filipp, J. M. Chow, and J. M. Gambetta, *Physical Review A* **93**, 012301 (2016).

[10] L. Chen, H.-X. Li, Y. Lu, C. W. Warren, C. J. Križan, S. Kosen, M. Rommel, S. Ahmed, A. Osman, J. Biznárová, *et al.*, *npj Quantum Information* **9**, 26 (2023).

[11] Walther-Meißner-Institut (WMI), *Annual Report 2024: 17-qubit superconducting chip entirely at the WMI facilities*, Annual Report (Bayernische Akademie der Wissenschaften / Technical University of Munich, 2024) describes a transmon-based 17-qubit processor with a planar lattice structure developed at WMI/TUM.

[12] J. J. Burnett, A. Bengtsson, M. Scigliuzzo, D. Niepce, M. Kudra, P. Delsing, and J. Bylander, *npj Quantum Information* **5**, 54 (2019).

[13] S. Kono, J. Pan, M. Chegnizadeh, X. Wang, A. Youssefi, M. Scigliuzzo, and T. J. Kippenberg, *Nature Communications* **15**, 3950 (2024).

[14] C. Müller, J. Lisenfeld, A. Shnirman, and S. Potoletto, *Physical Review B* **92**, 035442 (2015).

[15] M. Tuokkola, Y. Sunada, H. Kivijärvi, J. Albanese, L. Grönberg, J.-P. Kaikkonen, V. Vesterinen, J. Govenius, and M. Möttönen, *Nature Communications* **16**, 5421 (2025).

[16] P. V. Klimov, J. Kelly, Z. Chen, M. Neeley, A. Megrant, B. Burkett, R. Barends, K. Arya, B. Chiaro, Y. Chen, *et al.*, *Physical review letters* **121**, 090502 (2018).

[17] C. Müller, J. H. Cole, and J. Lisenfeld, *Reports on Progress in Physics* **82**, 124501 (2019).

[18] H. Paik, D. I. Schuster, L. S. Bishop, G. Kirchmair, G. Catelani, A. P. Sears, B. Johnson, M. Reagor, L. Frunzio, L. I. Glazman, *et al.*, *Physical review letters* **107**, 240501 (2011).

[19] P. Krantz, M. Kjaergaard, F. Yan, T. P. Orlando, S. Gustavsson, and W. D. Oliver, *Applied physics reviews* **6** (2019).

[20] A. Blais, A. L. Grimsmo, and A. Wallraff, *Reviews of Modern Physics* **93**, 025005 (2021).

[21] L. V. Abdurakhimov, I. Mahboob, H. Toida, K. Kakuyanagi, Y. Matsuzaki, and S. Saito, *PRX Quantum* **3**, 040332 (2022).

[22] S. Matityahu, A. Shnirman, and M. Schechter, *Physical Review Applied* **21**, 044055 (2024).

[23] B.-J. Liu, Y.-Y. Wang, T. Sheffer, and C. Wang, *Physical Review Letters* **133**, 160602 (2024).

[24] L. Chen, K.-H. Lee, C.-H. Liu, B. Marinelli, R. K. Naik, Z. Kang, N. Goss, H. Kim, D. I. Santiago, and I. Siddiqi, arXiv preprint arXiv:2503.04702 (2025).

[25] M. Scigliuzzo, A. Bengtsson, J.-C. Besse, A. Wallraff, P. Delsing, and S. Gasparinetti, *Physical Review X* **10**, 041054 (2020).

[26] D. S. Lvov, S. A. Lemziakov, E. Ankerhold, J. T. Peltonen, and J. P. Pekola, *Physical Review Applied* **23**, 054079 (2025).

[27] X. Jin, A. Kamal, A. Sears, T. Gudmundsen, D. Hover, J. Miloshi, R. Slattery, F. Yan, J. Yoder, T. Orlando, *et al.*, *Physical Review Letters* **114**, 240501 (2015).

[28] J. Biznárová, A. Osman, E. Rehman, L. Chayannun, C. Križan, P. Malmberg, M. Rommel, C. Warren, P. Delsing, A. Yurgens, *et al.*, *npj Quantum Information* **10**, 78 (2024).

[29] D. Colao Zanuz, Q. Ficheux, L. Michaud, A. Orekhov, K. Hanke, A. Flasby, M. Bahrami Panah, G. J. Norris, M. Kerschbaum, A. Remm, *et al.*, *Physical Review Applied* **23**, 044054 (2025).

[30] X. You, Z. Huang, U. Alyanak, A. Romanenko, A. Grassellino, and S. Zhu, *Physical Review Applied* **18**, 044026 (2022).

[31] D. M. Debroy, M. McEwen, C. Gidney, N. Shutty, and A. Zalcman, arXiv preprint arXiv:2410.14891 (2024).

[32] A. Dane, K. Balakrishnan, B. Wacaser, L.-W. Hung, H. Mamin, D. Rugar, R. M. Shelby, C. Murray, K. Rodbell, and J. Sleight, arXiv preprint arXiv:2503.12514 (2025).

[33] M. Bal, A. A. Murthy, S. Zhu, F. Crisa,

X. You, Z. Huang, T. Roy, J. Lee, D. v. Zanten, R. Pilipenko, *et al.*, npj Quantum Information **10**, 43 (2024).

[34] S. Simbierowicz, C. Shi, M. Collodo, M. Kirste, F. Hassani, J. Fink, J. Bylander, D. P. Lozano, and R. Lake, Bluefors Oy **8** (2021).

[35] S. De Graaf, L. Faoro, L. Ioffe, S. Mhashabde, J. Burnett, T. Lindström, S. Kurbatkin, A. Danilov, and A. Y. Tzalenchuk, Science Advances **6**, eabc5055 (2020).

[36] H. Kim, C. Jünger, A. Morvan, E. S. Barnard, W. P. Livingston, M. Altoé, Y. Kim, C. Song, L. Chen, J. M. Kreikebaum, *et al.*, Applied Physics Letters **121** (2022).

[37] J. R. Nesbitt and A. F. Hebard, Physical Review B—Condensed Matter and Materials Physics **75**, 195441 (2007).

[38] P. Koppinen, L. Väistö, and I. Maasilta, Applied physics letters **90** (2007).

[39] A. Bilmes, A. K. Händel, S. Volosheniuk, A. V. Ustinov, and J. Lisenfeld, Superconductor Science and Technology **34**, 125011 (2021).

[40] I. M. Pop, T. Fournier, T. Crozes, F. Lecocq, I. Matei, B. Pannetier, O. Buisson, and W. Guichard, Journal of Vacuum Science & Technology B **30** (2012).

[41] J. Koch, T. M. Yu, J. Gambetta, A. A. Houck, D. I. Schuster, J. Majer, A. Blais, M. H. Devoret, S. M. Girvin, and R. J. Schoelkopf, Physical Review A—Atomic, Molecular, and Optical Physics **76**, 042319 (2007).

[42] V. Ambegaokar and A. Baratoff, Physical review letters **10**, 486 (1963).

[43] M. Naghiloo, arXiv preprint arXiv:1904.09291 (2019).

[44] A. Greene, *Calibration and Utilization of High-Fidelity Two-Qubit Operations*, Ph.D. thesis, Massachusetts Institute of Technology (2023).

[45] Y. Y. Gao, M. A. Rol, S. Touzard, and C. Wang, PRX quantum **2**, 040202 (2021).

[46] A. D'Elia, B. Alfakes, A. Alkhazaleh, L. Banchi, M. Beretta, S. Carrazza, F. Chiarello, D. Di Gioacchino, A. Giachero, F. Henrich, *et al.*, Applied Sciences **14**, 1478 (2024).

[47] A. K. Syed, X. Zhang, J. E. Moffatt, and M. E. Fitzpatrick, International Journal of Fatigue **98**, 53 (2017).

[48] Z. Luo, T. Mayer, D. Zahn, C. M. Guizan, J. Weber, S. Lang, H. Bender, L. Schwarzenbach, L. Nebrich, R. Pereira, *et al.*, IEEE Microwave and Wireless Technology Letters (2025).

[49] H.-X. Li, D. Shiri, S. Kosen, M. Rommel, L. Chayanun, A. Nylander, R. Rehammar, G. Tancredi, M. Caputo, K. Grigoras, *et al.*, IEEE Transactions on Quantum Engineering **4**, 1 (2023).

## Supplementary information: Stability studies on subtractively-fabricated CMOS-compatible superconducting transmon qubits

### I. EXPERIMENT[S1–S3]

#### A. Pulses

To drive the qubits, we use pulses with Gaussian envelope. First, the pulse length is set (140 ns–200 ns), then the amplitude is varied in a Rabi experiment to calibrate the  $X_{180}$  and  $X_{90}$  gates. Readout uses rectangular pulses. We optimize the readout by performing single-shot readout experiment for different readout powers and choosing the parameters that maximize readout fidelity.

#### B. Pulse sequences and parameters extraction

**Fig. S1** illustrates the pulse sequences for lifetime measurement, Ramsey experiment, and single-shot readout. Each readout is followed by a passive reset (not shown in **Fig. S1**). In the following, we describe how the different parameters in Tab. II of the main text are extracted.

##### 1. Lifetime measurement

For each delay  $\tau$ , the pulse sequence shown in **Fig. S1.a,b** is executed on the qubit. After averaging over  $2^{10}$  repetitions, we obtain  $P_{|1\rangle}(\tau)$ , the excited-state population after delay  $\tau$  following excitation. By fitting  $P_{|1\rangle}(\tau)$  to an exponential decay:

$$P_{|1\rangle}(\tau) = A \cdot \exp\left(-\frac{\tau}{T_1}\right) + B \quad (\text{S1})$$

we obtain the lifetime of the qubit  $T_1 = 1/\Gamma_1$ .  $A$  and  $B$  are fitting parameters and  $\Gamma_1$  is the energy decay rate. Typically,  $A \approx 1$  and  $B \approx 0$ .

##### 2. Ramsey experiment

The Ramsey pulse sequence displayed in **Fig. S1.c,d** yields an oscillatory decay of  $P_{|1\rangle}(\tau)$  that follows the equation:

$$P_{|1\rangle}(\tau) = A \cdot \cos(2\pi f_{\text{Ramsey}} \tau + \phi_0) \exp\left(-\frac{\tau}{T_2^*}\right) + B \quad (\text{S2})$$

where  $A$ ,  $B$ , and  $\phi_0$  are fitting parameters,  $T_2^*$  is the effective transverse relaxation time, and

$f_{\text{Ramsey}}$  is the Ramsey oscillation frequency. Typically,  $A \approx B \approx 1/2$  and  $\phi_0 \approx 0$ .

Using  $f_{\text{Ramsey}} = f_q - f_{\text{Drive}}$ , where  $f_q$  and  $f_{\text{Drive}}$  are the qubit and the drive frequencies, respectively, we can calibrate the drive to the qubit frequency with high accuracy. However, due to the symmetry of the cosine function and  $\phi_0 \approx 0$ , a single Ramsey experiment ( $X_{90}$ -delay  $\tau$ - $X_{90}$ -readout) cannot determine the sign of  $f_{\text{Ramsey}}$ . This problem can be solved by either using a pulse sequence where the second pulse is  $Y_{90}$ , i.e.  $X_{90}$ -delay  $\tau$ - $Y_{90}$ -readout, or by introducing an additional detuning  $\Delta_f$ . Assuming the initial drive frequency is  $f_{\text{Drive},i} = f_q + \delta f$  and  $\Delta_f > |\delta f|$ , the possible values  $f_{\text{Ramsey}}$  takes are  $f_{\text{Ramsey}} = |\delta f| + \Delta_f$  or  $f_{\text{Ramsey}} = -|\delta f| + \Delta_f$ , which are both positive. The calibrated drive frequency  $f_{\text{Drive,cal}}$  is then:

$$f_{\text{Drive,cal}} = f_{\text{Drive},i} - (f_{\text{Ramsey}} - \Delta_f) \approx f_q \quad (\text{S3})$$

The introduced detuning also benefits our experiment, where we track the time evolution of  $f_{\text{Ramsey}}$ : Since the time span of a single experiment  $t_{\text{max}}$  is limited by decay or choice,  $f_{\text{Ramsey}}$  smaller than  $1/t_{\text{max}}$  cannot be detected. With detuning, frequency shifts are modulated around  $\Delta_f$ , increasing sensitivity to small drifts relative to the initial frequency. The detuning  $\Delta_f$  is implemented by adding a delay-dependent phase  $\phi(\tau)$  to the second pulse of the Ramsey sequence [S4–S6]:

$$\phi(\tau) = 2\pi\Delta_f \cdot \tau \bmod(2\pi) \quad (\text{S4})$$

This operation is denoted in **Fig. S1.d** by the gate  $R_z(\phi)$ . According to the Nyquist theorem, undersampling is possible if  $f_q$  shifts significantly [S7]. However, the time span must be large enough to capture  $T_2^*$  accurately, creating a trade-off between measurement speed and sampling rate. Ideally, the sampling rate and detuning would dynamically adapt to the evolution of  $f_{\text{Ramsey}}$  (not implemented in this work). **Tab. S1** presents the measurements parameters for each qubit. The time spans are chosen to satisfy  $t_{\text{max}} \approx 5T_2^*$ .

##### 3. Single-shot readout

Using the setup depicted in **Fig. S1.e,f**, we obtain two blobs in the IQ plane, e.g. **Fig. S3.a**, each corresponding to a qubit state. We compute the centers (means) of the two blobs and the

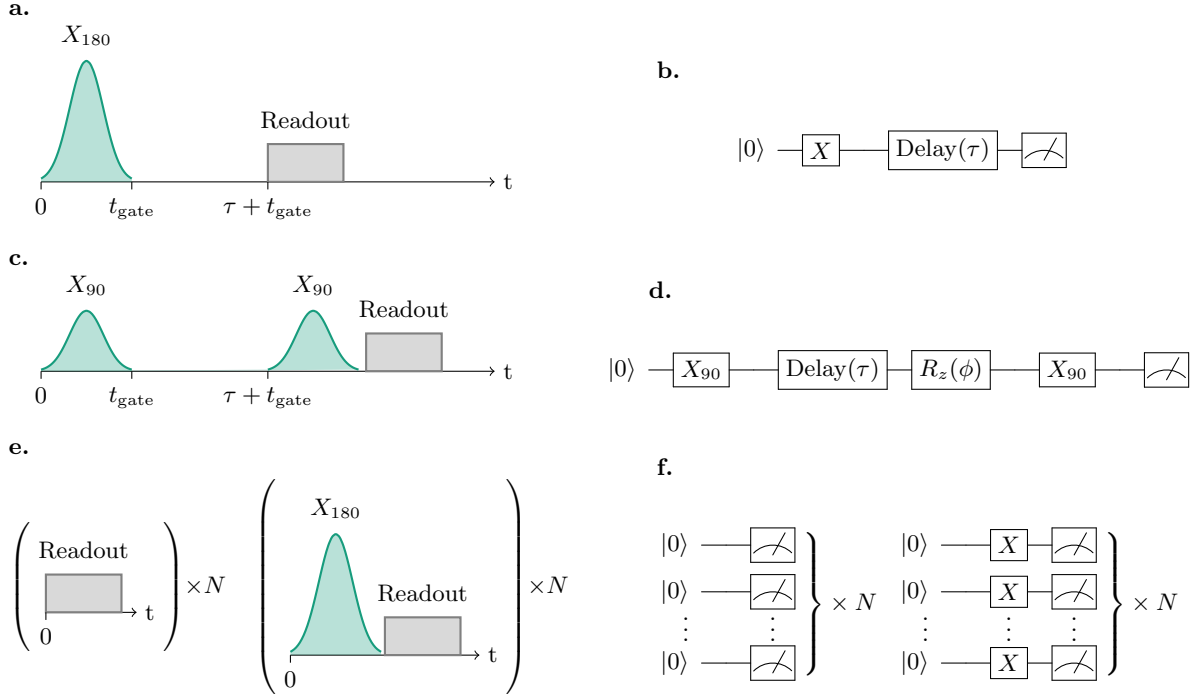


Fig. S1. Pulse sequences for qubit characterization. Left panels show pulse-level implementation; right panels show equivalent quantum circuit representations. a,b) lifetime measurement. c,d) Ramsey sequence with virtual  $R_z(\phi)$  for frequency detuning. e,f) Single-shot readout with  $N$  repetitions of  $|0\rangle$  and  $|1\rangle$  measurements

Qubit	$t_{\max}$	$f_{\text{Nyquist}}$	Detuning	$\langle T_2^* \rangle$
A.1	120	166.7	20	28.56
A.2	250	80	10	51.26
A.3	200	100	10	38.88
A.4	150	133.3	10	34.96
B.1	150	133.3	15	39.38
B.2	250	80	10	44.15
B.3	250	80	15	44.03
B.4	100	200	15	15.96

Tab. S1. Ramsey measurement parameters. Time values are given in  $\mu\text{s}$  and frequency values are given in kHz. For A.1, only the first valid values of  $T_2^*$  were averaged. For the other qubits,  $\langle T_2^* \rangle$  is obtained by fitting the distributions. The dropout of B.1 was excluded from the fit.

distance separating them,  $\Delta_m$ . To calculate the readout fidelity  $\mathcal{F}$  and effective qubit temperature  $T_{\text{eff}}$ , we first perform a state discrimination. In this work, we use Quadratic Discriminant Analysis (QDA). The IQ plane is divided into two regions, each representing a state. The readout fidelity  $\mathcal{F}$  is then [S8, S9]:

$$\begin{aligned} \mathcal{F} &= \frac{P(|1\rangle|1\rangle) + P(|0\rangle|0\rangle)}{2} \\ &= 1 - \frac{P(|0\rangle|1\rangle) + P(|1\rangle|0\rangle)}{2} \end{aligned} \quad (\text{S5})$$

where  $P(|i\rangle|j\rangle)$  is the probability of finding the qubit in the region corresponding to the state  $|i\rangle$  after being prepared to the state  $|j\rangle$ . The effective qubit temperature  $T_{\text{eff}}$  can be estimated from  $P(|1\rangle|0\rangle)$  and  $P(|0\rangle|0\rangle)$ . After preparing the qubit in the state  $|0\rangle$ , the transition  $|0\rangle \rightarrow |1\rangle$  is possible, e.g. due to thermal excitation by photons at the qubit frequency  $f_q$  or hot non-equilibrium quasiparticles. We can determine the effective qubit temperature through the Boltzmann-Maxwell distribution: [S10–S13]:

$$\frac{P(|1\rangle|0\rangle)}{P(|0\rangle|0\rangle)} = \exp\left(-\frac{h f_q}{k_B T_{\text{eff}}}\right) \quad (\text{S6})$$

which gives:

$$T_{\text{eff}} = -\frac{h f_q}{k_B \cdot \ln\left(\frac{P(|1\rangle|0\rangle)}{P(|0\rangle|0\rangle)}\right)} \quad (\text{S7})$$

where  $h$  is the Planck constant and  $k_B$  is the Boltzmann constant. The term  $P(|0\rangle|0\rangle)$  in Eq. S7 can be approximated as  $P(|0\rangle|0\rangle) = 1 - P(|1\rangle|0\rangle) \approx 1$  since typically  $P(|1\rangle|0\rangle) \ll 1$ . An increase in  $P(|1\rangle|0\rangle)$  reflects in a decrease of  $\mathcal{F}$  and an increase of  $T_{\text{eff}}$ , giving an anti-correlation between  $T_{\text{eff}}$  and  $\mathcal{F}$ .

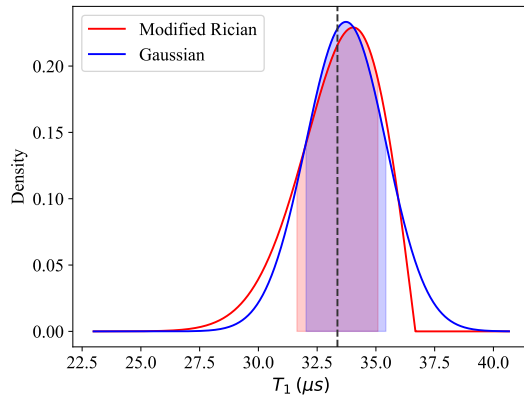


Fig. S2. Comparison of Gaussian (blue) and modified Rician (red) distributions for fitting. The modified Rician fit follows Eq. S9. Both distributions are fitted to  $T_1$ -data from qubit A.4. The shaded areas represent one standard deviation intervals around the mean. The vertical dotted line indicates the mean of the modified Rician distribution.

## II. SINGLE-COOLDOWN STABILITY

### A. Results from qubits other than A.2

In this section, we present additional results in a manner similar to Fig.3 of the main manuscript. Fig. S5 corresponds to qubit A.1, where the Ramsey results were omitted due to the aforementioned strong abrupt frequency change. Fig. S6 and Fig. S7 display the measurement results for qubits A.3 and A.4, respectively. Fig. S8 shows the temporal evolution of parameters of B.1, with the time interval of the strongest dropout indicated by dotted lines. Fig. S9 shows the measurements results for B.2, with the particularity of a correlation between  $\Delta_m$  and  $\mathcal{F}$ . In Fig. S10 corresponding to B.3, we can observe the fluctuations in  $\Delta_m$  (see section II C 1). Fig. S11 displays the evolution of B.4 parameters. Interestingly, the two major frequency jumps coincide with jumps in  $T_2^*$ .

### B. Rician fit

Due to the skewness of the distributions, we implement a modified Rician fit: mirrored and with an offset. The standard Rician distribution is described by the probability density function[S14]:

$$f_{\nu,\sigma}(x) = \frac{x}{\sigma^2} \exp\left(\frac{-(x^2 + \nu^2)}{2\sigma^2}\right) I_0\left(\frac{x\nu}{\sigma^2}\right) ; x > 0 \quad (S8)$$

where  $I_0$  is the modified Bessel function of the first kind of order zero, and  $\sigma$  and  $\nu$  are the distribution parameters. For our fit function, we

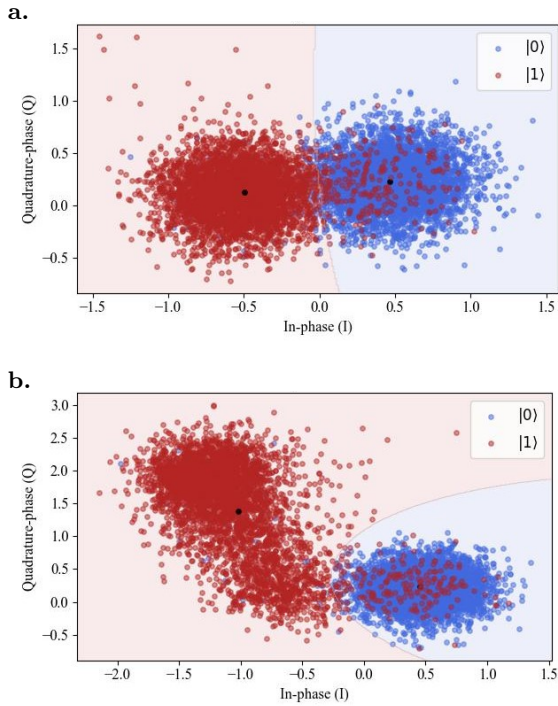


Fig. S3. Two single-shot readout measurements of qubit B.3. a) Measurement with two well-defined blobs corresponding to states  $|0\rangle$  (blue) and  $|1\rangle$  (red), representing the expected result for a two-level-system. The black dots represent the centers of the blobs used to calculate  $\Delta_m$ . b) Measurement-induced state transitions, where the red points (excited state) spread over the IQ plane, instead of forming a Gaussian blob. After state discrimination, we find that the result for  $\Delta_m$  is almost double compared with (a).

use:

$$f_{T_i}(t) = f_{\nu,\sigma}(T_{i,\max} - t) ; t \leq T_{i,\max} \quad (S9)$$

where  $T_i$  can be  $T_1$  or  $T_2^*$  and  $T_{i,\max}$  is an additional fit parameter representing the offset and maximum value  $T_i$  can achieve. Fig. S2 shows a comparison between a Gaussian and a modified Rician distribution (following Eq. S9) with parameters extracted from the results of qubit A.4. The choice of the fit function in Eq. S9 is purely empirical and is not based on an established physical model. Other asymmetric distributions could also be used to model the distribution of coherence and dephasing times.

### C. Sources of fluctuations

#### 1. Measurement-induced state transitions

In this section, we discuss the fluctuations in  $\Delta_m$  experienced by B.3. Fig. S3.a and Fig. S3.b

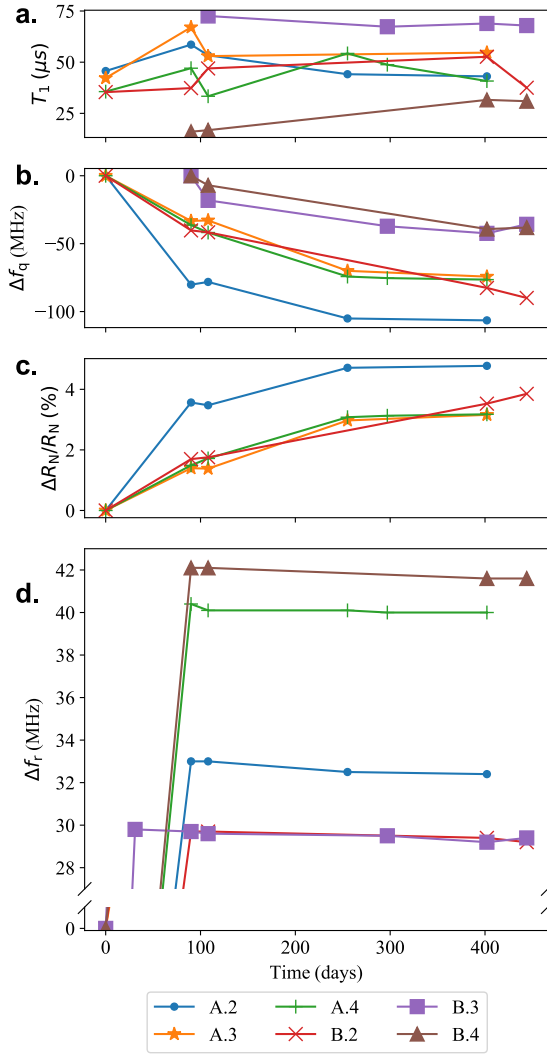


Fig. S4. Evolution over multiple cooldown cycles of a)  $T_1$  and of b) qubit frequency shifts  $\Delta f_q$  and d) readout frequency shifts  $\Delta f_r$  for qubits A.2-4 and B.2-4. c) Evolution of estimated  $\Delta R_N/R_N$ . Frequency and  $T_1$  measurements for qubits B.3 and B.4 during the first cooldown are unavailable. That is why both qubits are not handled in panel (c). The zero-time point refers to the same first cooldown in Fig.6 of the main text.

show the results of two separate single-shot measurements performed on B.3, the first with a low  $\Delta_m$  and the second with high  $\Delta_m$ . Fig. S3.a (low  $\Delta_m$ ) corresponds to the expected result for a two-level system. In Fig. S3.b, we observe that measurement points prepared in the excited state spread over the IQ plane, moving the IQ blobs away from each other and increasing  $\Delta_m$ . This behavior could be attributed to measurement-induced state transitions[S15–S17], also referred to as ionization[S16, S17], which occurs when certain numbers of photons are present in the

resonator cavity. In this scenario, the spread of the excited state blob could be the result of the qubit decaying back to the first excited state. We hypothesize that the sudden switching between the two cases (Fig. S3.a and Fig. S3.b) and consequently the  $\Delta_m$  fluctuations could be due to fluctuations in the photon number in the readout cavity.

## 2. TLS-qubit interaction

The model introduced in Ref.[S18] states the following equations:

$$\langle \Gamma_{1,\text{tot}} \rangle = N_{\text{TLS}} \langle \Gamma_{1,\text{single-TLS}} \rangle \quad (\text{S10})$$

$$\text{Var}(\Gamma_{1,\text{tot}}) = N_{\text{TLS}} \text{Var}(\Gamma_{1,\text{single-TLS}}) \quad (\text{S11})$$

where  $N_{\text{TLS}}$  is the TLS density,  $\Gamma_{1,\text{single-TLS}}$  is the decay rate of the qubit under the influence of a single TLS, and  $\Gamma_{1,\text{tot}}$  is the decay rate due to a TLS ensemble. Var denotes the variance. To derive the equation Eq. 1 of the main text, we use:

$$\langle \Gamma_{1,\text{tot}} \rangle = 1/\langle \Gamma_{1,\text{tot}} \rangle \quad (\text{S12})$$

and

$$\text{Var}(\Gamma_{1,\text{tot}}) \approx \text{Var}(\Gamma_{1,\text{tot}})/\langle \Gamma_{1,\text{tot}} \rangle^4 \quad (\text{S13})$$

This yields:

$$\begin{aligned} \text{Var}(\Gamma_{1,\text{tot}}) &= N_{\text{TLS}} \text{Var}(\Gamma_{1,\text{single-TLS}})/\langle \Gamma_{1,\text{tot}} \rangle^4 \\ &= \frac{\langle \Gamma_{1,\text{tot}} \rangle \cdot \text{Var}(\Gamma_{1,\text{single-TLS}})}{\langle \Gamma_{1,\text{single-TLS}} \rangle \cdot \langle \Gamma_{1,\text{tot}} \rangle^4} \\ &= \frac{\text{Var}(\Gamma_{1,\text{single-TLS}})}{\langle \Gamma_{1,\text{single-TLS}} \rangle} \cdot \langle \Gamma_{1,\text{tot}} \rangle^3 \end{aligned} \quad (\text{S14})$$

Consequently:

$$\begin{aligned} \sigma_{T_1} &= \sqrt{\text{Var}(T_1)} \\ &= \sqrt{\frac{\text{Var}(\Gamma_{1,\text{single-TLS}})}{\langle \Gamma_{1,\text{single-TLS}} \rangle}} \cdot \langle \Gamma_{1,\text{tot}} \rangle^{3/2} \quad (\text{S15}) \\ &:= a \langle \Gamma_{1,\text{tot}} \rangle^{3/2} \end{aligned}$$

## III. LONG-TERM STABILITY (OVER SEVERAL COOLDOWNS)

In Fig. S4 we present the rest of the aging data for qubits other than A.1 and B.1. B.3 and B.4 frequency and  $T_1$  measurements during the first cooldown are not available. The remaining qubits exhibit similar behavior as described in the main text.

---

[S1] P. Krantz, M. Kjaergaard, F. Yan, T. P. Orlando, S. Gustavsson, and W. D. Oliver, *Applied physics reviews* **6** (2019).

[S2] Zurich Instruments, [Efficient generation of dynamic pulses](#) (2023), accessed: 2024-09-05.

[S3] M. Naghiloo, arXiv preprint arXiv:1904.09291 (2019).

[S4] N. F. Ramsey, *Physical Review* **78**, 695 (1950).

[S5] M. Shuker, J. Pollock, R. Boudot, V. Yudin, A. Taichenachev, J. Kitching, and E. A. Donley, *Physical Review Letters* **122**, 113601 (2019).

[S6] C. Roos, M. Chwalla, T. Monz, P. Schindler, K. Kim, M. Riebe, and R. Blatt, in *Laser Spectroscopy* (World Scientific, 2008) pp. 53–62.

[S7] C. Shannon, *Proceedings of the IRE* **37**, 10 (1949).

[S8] E. Magesan, J. M. Gambetta, A. D. Córcoles, and J. M. Chow, *Physical review letters* **114**, 200501 (2015).

[S9] L. Chen, H.-X. Li, Y. Lu, C. W. Warren, C. J. Križan, S. Kosen, M. Rommel, S. Ahmed, A. Osman, J. Biznárová, *et al.*, *npj Quantum Information* **9**, 26 (2023).

[S10] S. Valenzuela, W. Oliver, D. Berns, K. Berggren, L. Levitov, and T. Orlando, in *APS March Meeting Abstracts* (2007) pp. J33–009.

[S11] K. Serniak, M. Hays, G. De Lange, S. Diamond, S. Shankar, L. Burkhart, L. Frunzio, M. Houzet, and M. Devoret, *Physical review letters* **121**, 157701 (2018).

[S12] D. S. Lvov, S. A. Lemziakov, E. Ankerhold, J. T. Peltonen, and J. P. Pekola, *Physical Review Applied* **23**, 054079 (2025).

[S13] X. Jin, A. Kamal, A. Sears, T. Gudmundsen, D. Hover, J. Miloshi, R. Slattery, F. Yan, J. Yoder, T. Orlando, *et al.*, *Physical Review Letters* **114**, 240501 (2015).

[S14] A. Abdi, C. Tepedelenlioglu, M. Kaveh, and G. Giannakis, *IEEE Communications Letters* **5**, 92 (2001).

[S15] T. Connolly, P. D. Kurilovich, V. D. Kurilovich, C. G. Böttcher, S. Hazra, W. Dai, A. Z. Ding, V. R. Joshi, H. Nho, S. Diamond, *et al.*, arXiv preprint arXiv:2506.05306 (2025).

[S16] M. F. Dumas, B. Groleau-Paré, A. McDonald, M. H. Muñoz-Arias, C. Lledó, B. D’Anjou, and A. Blais, *Physical Review X* **14**, 041023 (2024).

[S17] R. Shillito, A. Petrescu, J. Cohen, J. Beall, M. Hauru, M. Ganahl, A. G. Lewis, G. Vidal, and A. Blais, *Physical Review Applied* **18**, 034031 (2022).

[S18] X. You, Z. Huang, U. Alyanak, A. Romanenko, A. Grassellino, and S. Zhu, *Physical Review Applied* **18**, 044026 (2022).

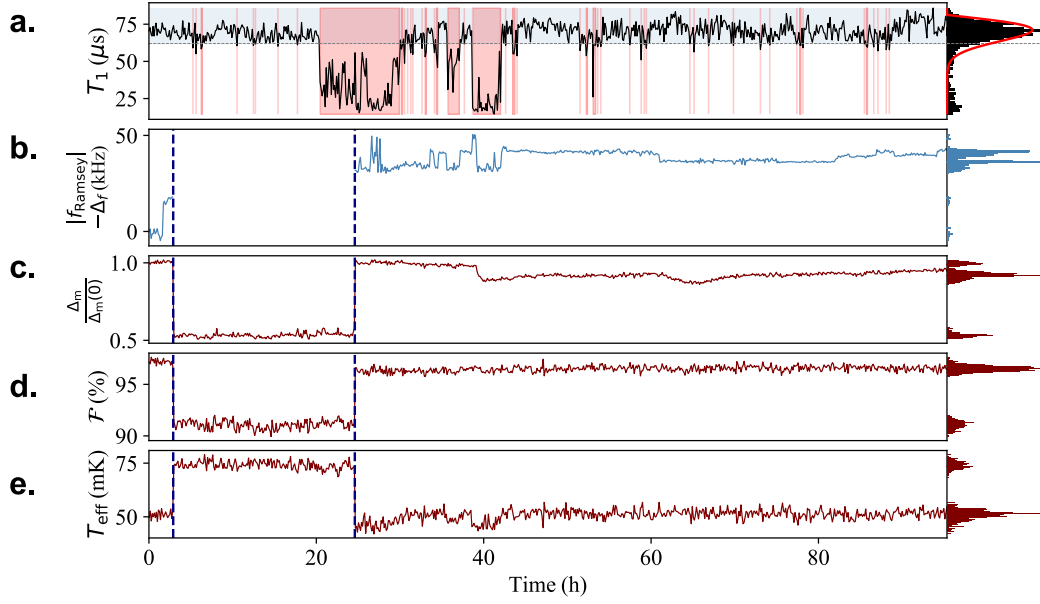


Fig. S5. Temporal evolution of qubit A.1 parameters.  $T_2^*$  measurements are omitted due to inadequate detuning or measurement time span, making the fits of  $T_2^*$  unreliable. The blue dashed lines highlight the period where  $T_2^*$  dropped significantly, in addition to deterioration of the readout and the effective temperature. Due to the  $T_2^*$  decrease, the frequency could not be fitted during this period.

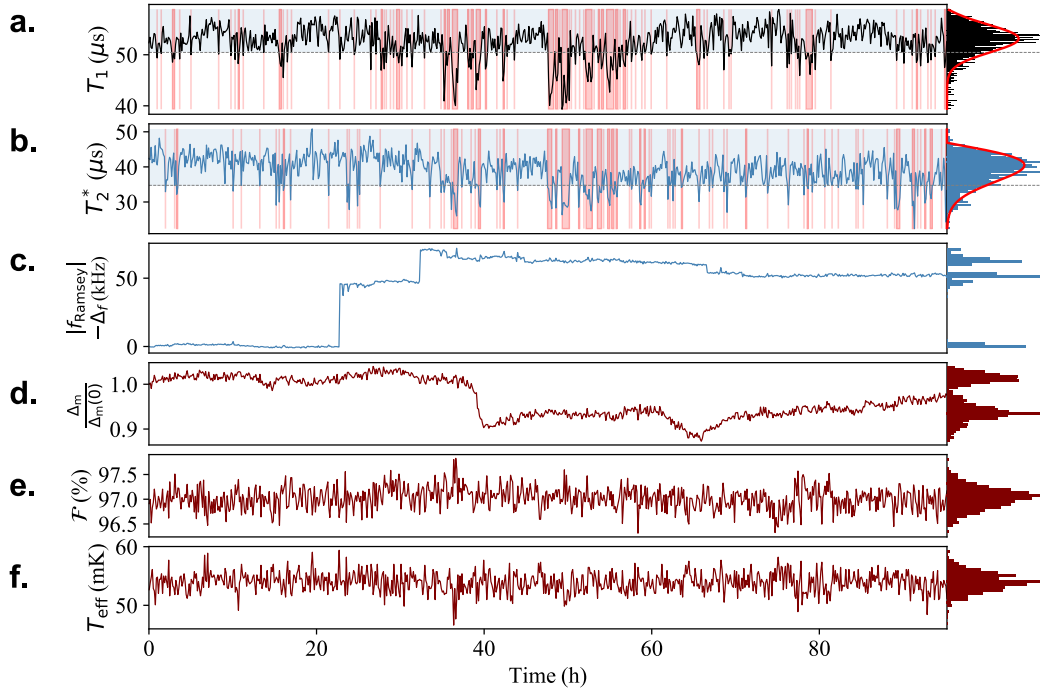


Fig. S6. Temporal evolution of qubit A.3 parameters

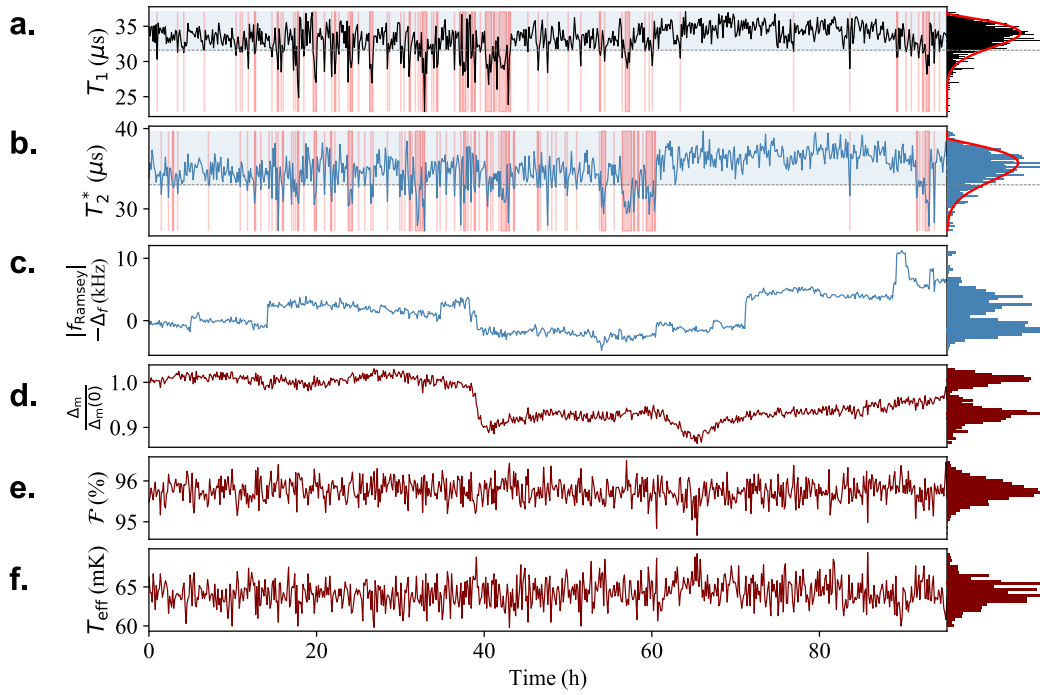


Fig. S7. Temporal evolution of qubit A.4 parameters

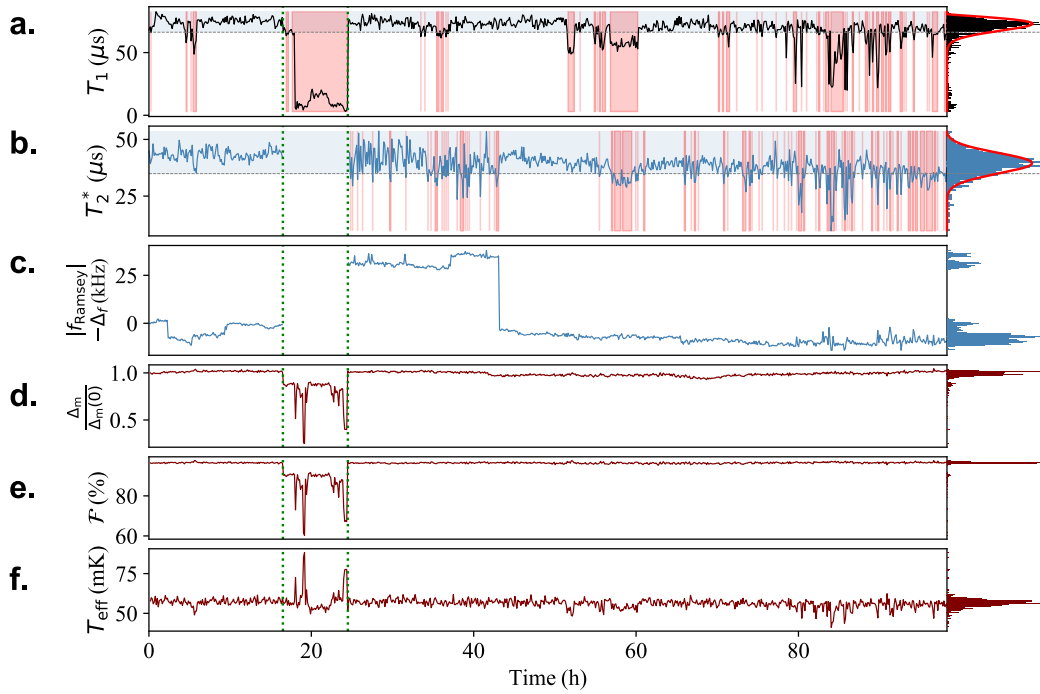


Fig. S8. Temporal evolution of qubit B.1 parameters. Dotted lines indicate the time interval of the strongest dropout.

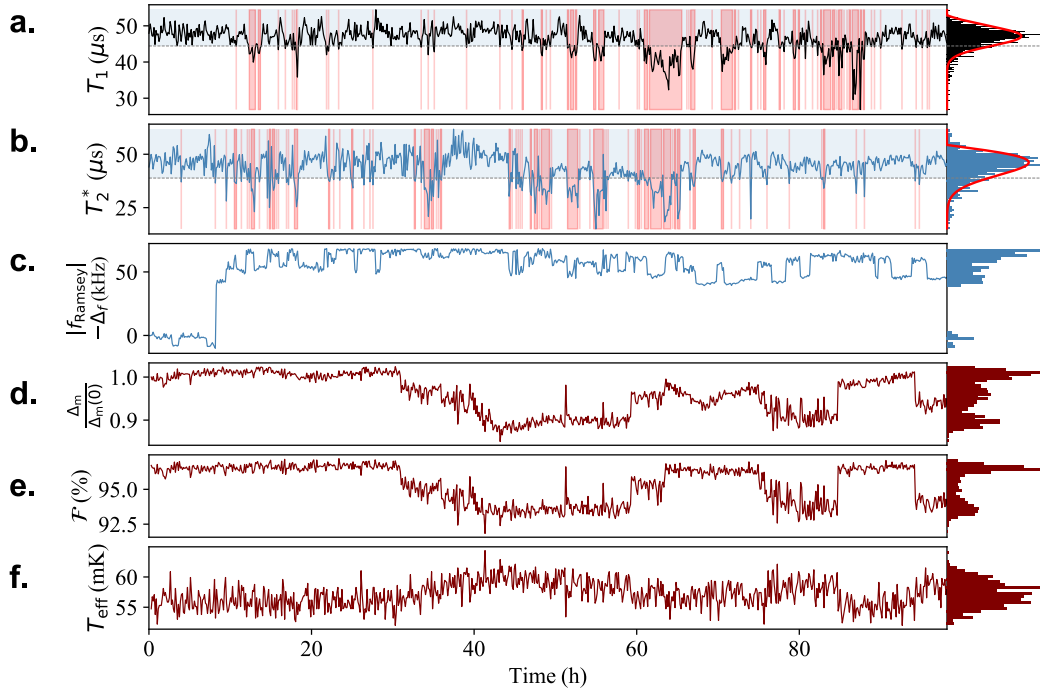


Fig. S9. Temporal evolution of qubit B.2 parameters. Note the correlation between  $\Delta_m$  and  $F$ .

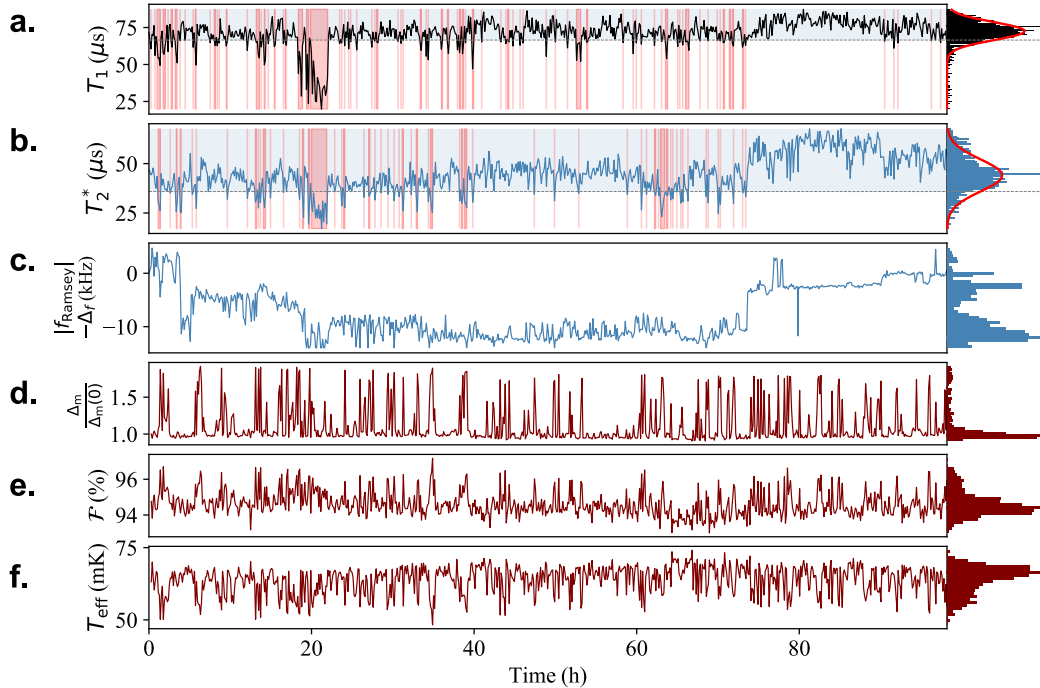


Fig. S10. Temporal evolution of qubit B.3 parameters, with strong fluctuations in  $\Delta_m$

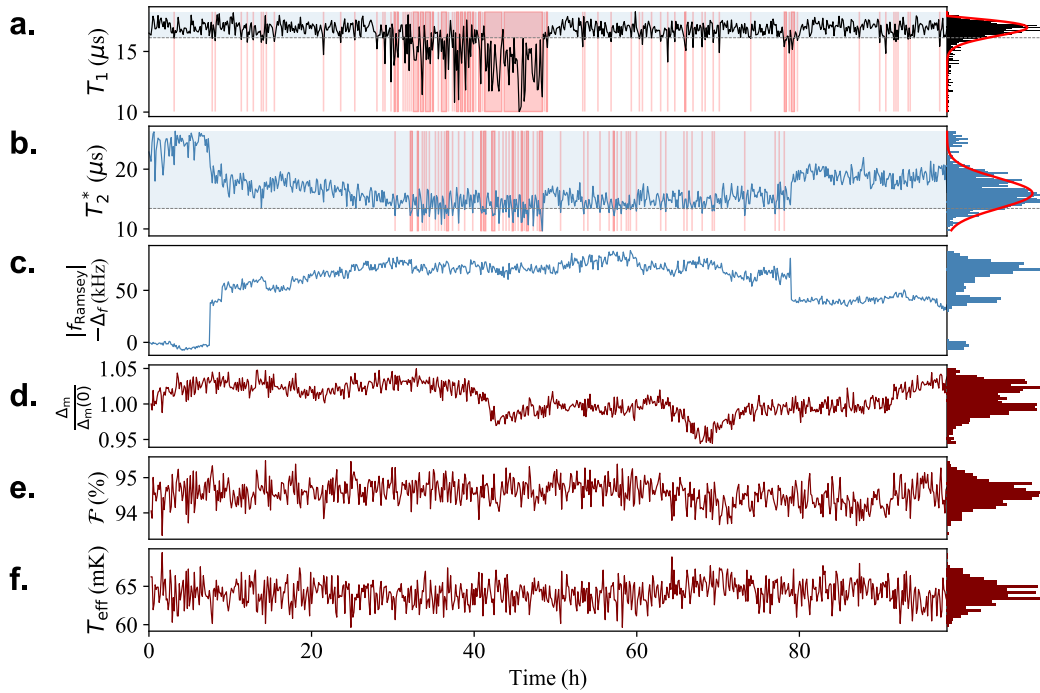


Fig. S11. Temporal evolution of qubit B.4 parameters. The two major frequency jumps coincide with jumps in  $T_2^*$